Ceramics International 44 (2018) 8684–8690

Contents lists available at ScienceDirect

Ceramics International

journal homepage: www.elsevier.com/locate/ceramint

The effects of Ga^{3+} substitution on local structure and photoluminescence of $Tb_3Al_5O_{12}$:Ce garnet phosphor

Jun Bi[a,b,c], Xuejiao Wang[d,*], Maxim S. Molokeev[e,f,g], Qi Zhu[a,b], Xiaodong Li[a,b], Jialin Chen[c], Xudong Sun[a,b], Byung-Nam Kim[h], Ji-Guang Li[a,b,h,**]

[a] Key Laboratory for Anisotropy and Texture of Materials (Ministry of Education), Northeastern University, Shenyang, Liaoning 110819, China
[b] Institute of Ceramics and Powder Metallurgy, School of Materials Science and Engineering, Northeastern University, Shenyang, Liaoning 110819, China
[c] State Key Laboratory of Advanced Technologies for Comprehensive Utilization of Platinum Metals, Kunming Institute of Precious Metal, Kunming, Yunnan 650106, China
[d] College of New Energy, Bohai University, New Songshan District, Jinzhou, Liaoning 121013, China
[e] Laboratory of Crystal Physics, Kirensky Institute of Physics, Federal Research Center KSC SB RAS, Krasnoyarsk 660036, Russia
[f] Department of Physics, Far Eastern State Transport University, Khabarovsk 680021, Russia
[g] Siberian Federal University, Krasnoyarsk 660041, Russia
[h] Research Center for Functional Materials, National Institute for Materials Science, 1-1 Namiki, Tsukuba, Ibaraki 305-0044, Japan

ARTICLE INFO

Keywords:
TbAG:Ce
Ga doping
Crystal structure
Photoluminescence

ABSTRACT

$(Tb_{0.985}Ce_{0.015})_3(Al_{1-x}Ga_x)_5O_{12}$ garnet phosphors (x = 0, 0.1, 0.2, 0.3, and 1.0) were prepared by calcining their coprecipitated precursors in air at 1500 °C, followed by reduction in hydrogen at 1200 °C. Rietveld refinement of the XRD results suggested that the Ga dopant predominantly resides at the octahedral Al site of the garnet lattice. Ga doping led to linearly expanded lattice constant, cell volume and theoretical density of the garnet compound and successively lower intensity and longer average fluorescence lifetime of the ~ 570 nm emission of Ce^{3+}. Blue shifted emission and $4f(^2F_{5/2})\rightarrow5d_1(E_{2g})$ excitation and red shifted $4f(^2F_{5/2})\rightarrow5d_2(E_{2g})$ excitation were also observed for the Ce^{3+} activator at a higher Ga content. The phenomena were interpreted by considering the band structure of the host, distortion of the CeO_8 polyhedron, and centroid shift and field splitting of the Ce^{3+} 5d energy levels.

1. Introduction

Inorganic scintillator is a ceramic material that emits ultraviolet or visible light under high energy radiation, and is finding wide applications in the multi-faceted areas of astrophysics, nuclear physics, security examination, geophysical and resources exploration, medical imaging, and so forth [1,2]. Oxide materials with the garnet structure are promising scintillator matrixes, due to their structure stability, good light-yield, non-hygroscopicity, optical transparency, readiness of activator doping, and excellent mechanical properties [3]. In practice, scintillators based on the garnet compounds of optically inert Y, Gd and Lu ions receive the most concerns [4–6]. Transparent ceramics have the advantages of low cost, isotropy and better processability, and thereby become powerful competitors of single crystal scintillators. Currently the main types of polycrystalline ceramic scintillators incorporate $(Y,Gd)_2O_3$:Eu and Lu_2O_3:Eu sesquioxides, Gd_2O_2S:Pr oxysulfide, and $Y_3Al_5O_{12}$:Ce (YAG:Ce) and $(Gd,RE)_3(Al,Ga)_5O_{12}$:Ce (RE = Y or Lu) garnets [7,8]. YAG:Ce scintillator shows excellent scintillation properties including high efficiency and fast decay [7], but its low theoretical density weakens the power to stop high-energy particles and thus leads to large size of the scintillation device. $Tb_3Al_5O_{12}$ (TbAG) has been a subject of considerable interest during recent years. Benefitted from its large Verdet constant and good optical transparency [9–11], TbAG crystals are widely used as Faraday isolators in many contemporary laser systems to prevent the optical feedback that leads to parasitic oscillation and frequency instability [12]. In the powder form, TbAG:Ce is well known as a yellow phosphor. Compared with YAG:Ce, the Tb^{3+} ions produce a stronger crystal field effect, which gives rise to yellow emission of a longer wavelength and is thus better suited for warm-light indoor illumination when combined with InGaN blue-LED chips [13,14]. As an optically active ion, the Tb^{3+} in the TbAG matrix generates complicated energy processes via interacting with the Ce^{3+} activator [15,16], and the observed matrix activation could be well suited for the high-energy excitation useful in scintillators.

In garnet scintillators, it is well known that trapping of free carriers by the intrinsic point defects of vacancies, antisites and dislocations

* Correspondence to: Bohai University, China.
** Correspondence to: National Institute for Materials Science, Japan.
E-mail addresses: wangxuejiao@bhu.edu.cn (X. Wang), li.jiguang@nims.go.jp (J.-G. Li).

https://doi.org/10.1016/j.ceramint.2018.02.104
Received 23 January 2018; Received in revised form 11 February 2018; Accepted 11 February 2018
Available online 12 February 2018

degrades scintillation performance. In order to overcome the problem, strategies have been proposed to remove or at least reduce the concentration of such defects, which is called “defect engineering”. Such operations, however, frequently bring about little effects since the formation energy of such defects is low and the cation antisites are charge neutral and therefore cannot be removed via the aliovalent doping technique that leads to defect annihilation [17]. Another strategy is to eliminate the impact of defects by modifying the band structure of the host lattice, which is called “bandgap engineering”. Tuning the band structure of $(Gd,RE)_3(Al,Ga)_5O_{12}$ garnet via Ga doping has been proved successful [18,19]. It was reported that the Ga^{3+} dopant may narrow the bandgap by pushing down the bottom of the conduction band [20], and, as a result, the antisite shallow traps can be enveloped by the conduction band edge [21]. Besides, substituting a part of Al with Ga considerably increases the density of garnet matrix, which is beneficial to scintillation purposes. Meanwhile, Ga doping may affect photoluminescence of the Ce^{3+} activator in the garnet host through modifying the $5d_1$ excited state of Ce^{3+} and also the energy gap between the bottom of the conduction band and the $5d_1$ energy level [18,19].

We synthesized in this work $Tb_3(Al_{1-x}Ga_x)_5O_{12}$:Ce solid-solution phosphors (x = 0, 0.1, 0.2, 0.3 and 1.0) by calcining their coprecipitated precursors, and the effects of Ga substitution on crystal structure and photoluminescence were investigated in detail. The observed luminescent properties were also interpreted with the band structure of the host, crystal field splitting and centroid shift of the Ce^{3+} energy levels, the local structure information deduced via Rietveld refinement, and the Ga^{3+} dopant itself. In the following sections, we report the powder synthesis, structure characterization, and photoluminescent properties of the series of phosphors.

2. Experiment procedure

The precursors for $(Tb_{0.985}Ce_{0.015})_3(Al_{1-x}Ga_x)_5O_{12}$ phosphors (x = 0, 0.1, 0.2, 0.3 and 1.0) were synthesized via coprecipitation with ammonium bicarbonate as the precipitant and nitrate as the cation source, and the details of which can be found elsewhere [22]. The concentration of Ce^{3+} activator was fixed at 1.5 at% in this work, since the value was previously found to be the optimal for Ce^{3+} luminescence in TbAG [16]. For phosphor synthesis, the precursor powders were calcined in air at 1500 °C for 4 h, followed by reducing in flowing hydrogen (2 L/min) at 1200 °C for 2 h to prevent Ce^{3+} and Tb^{3+} oxidation.

The phase structure of the garnet powder was analyzed via x-ray diffractometry (XRD, PANALYTICAL B.V, Model PW3040/60, Almelo, Netherlands) under 40 kV/40 mA, using nickel filtered CuKα radiation (λ = 0.15406 nm). Diffraction data were collected in the step-scan mode, with a step size of 2θ = 0.033° and an accumulation time of 1 s per step. Particle morphology was observed via field-emission scanning electron microscopy (FE-SEM, Model 1006123, Czech Republic). Emission and excitation properties of the phosphors were measured at room temperature with an FP-8600 fluorospectrophotometer (JASCO, Japan) that is equipped with a 150 W Xe-lamp as the excitation source and a Φ60 mm intergating sphere (ISF-513, JASCO, Japan). Monochromatization of the excitation and emission lights was achieved with a Rowland concave grating (1800 grooves/mm). The optical measurements were operated under identical conditions for all the phosphors synthesized in this work, with a scanning speed of 100 nm/min, a response time of 0.5 s, sensitivity of $S/N \geq 200$, and slit widths of 5 nm for both excitation and emission. The spectral response of the spectrophotometer was corrected with a Rhodamine-B solution (5.5 g L^{-1} in ethylene glycol) and a standard light source unit (ECS-333, JASCO, Japan) for the ranges of 220–600 nm and 350–850 nm, respectively. Fluorescence decay kinetics were measured at room temperature on a HORIBA scientific modular fluorescence lifetime system (Model DeltaFlex, HORIBA Jobin Yvon IBH Ltd., Scotland), using NanoLED-455 (λ = 450 nm, 1.4 ns pulse duration) as the excitation source.

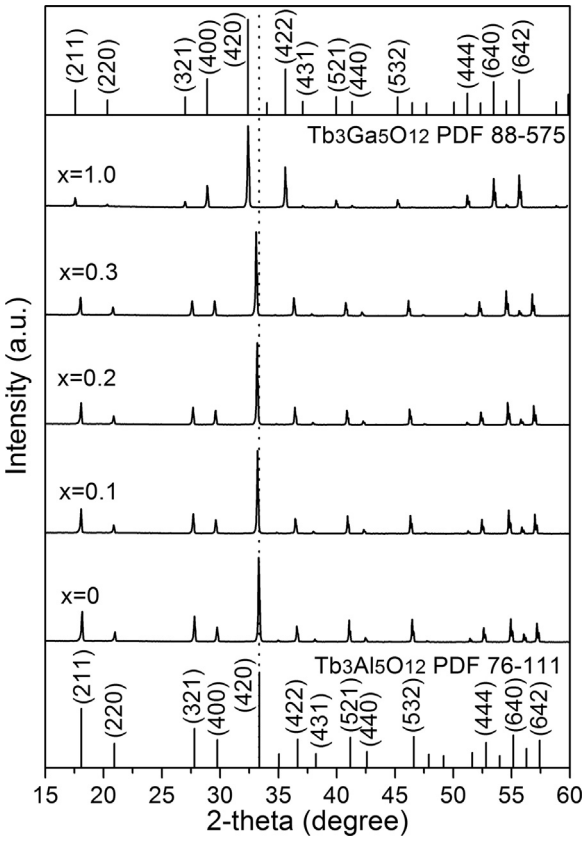

Fig. 1. XRD patterns of the $(Tb_{0.985}Ce_{0.015})_3(Al_{1-x}Ga_x)_5O_{12}$ phosphor powders. The standard diffractions of $Tb_3Al_5O_{12}$ (JCPDS no. 76-111) and $Tb_3Ga_5O_{12}$ (JCPDS no. 88-575) are included as bars for comparison.

3. Results and discussion

3.1. Phase structure and morphology of the phosphors

Fig. 1 shows XRD patterns of the resultant $(Tb_{0.985}Ce_{0.015})_3(Al_{1-x}Ga_x)_5O_{12}$ phosphors, where it is seen that the Ga doped samples (x = 0, 0.1, 0.2 and 0.3) can basically be indexed with $Tb_3Al_5O_{12}$ (JCPDS No. 76–111) while the $(Tb_{0.985}Ce_{0.015})_3Ga_5O_{12}$ powder (x = 1.0) is well indexable with $Tb_3Ga_5O_{12}$ (JCPDS no. 88-575). Ga doping shifts the diffraction peaks towards smaller angles, indicating expanded unit cell of the garnet structure. Rietveld refinement (Fig. 2) was performed using the TOPAS 4.2 software [23], and indeed all the diffraction peaks can be indexed by the cubic cell of garnet (*Ia*-3*d*), with cell parameters close to that (12.0 Å, JCPDS no. 76-111) of $Tb_3Al_5O_{12}$ (Table 1). The crystal structure of TbAG was thus taken as the starting model for Rietveld refinement. The Tb site is occupied by Tb^{3+} ions with the fixed occupancy of p = 0.985 and by Ce^{3+} ions with p = 0.015. The Al site is occupied by Al^{3+} and Ga^{3+}, whose occupancies are in accordance with the chemical formula of $(Tb_{0.985}Ce_{0.015})_3(Al_{1-x}Ga_x)_5O_{12}$. In the refinement, Tb and Ce ions were set to have the same thermal parameters and also the Ga and Al ions to reduce the total number of refined parameters. Refinement is stable and gave low *R*-factors (Table 1). The derived coordinates of atoms and main bond lengths are presented in Tables S1 and 2, respectively.

Fig. 3a shows that the cell volume of $(Tb_{0.985}Ce_{0.015})_3(Al_{1-x}Ga_x)_5O_{12}$ linearly increases with increasing x, which is consistent with the fact that Ga^{3+} (0.47 Å for CN = 4) is bigger in ionic radius than Al^{3+} (0.39 Å for CN = 4) [24]. The d(Al1/Ga1-O) bond length also shows noticeable increase with increasing x (Table 2 and Fig. 3b), but d(Al2/

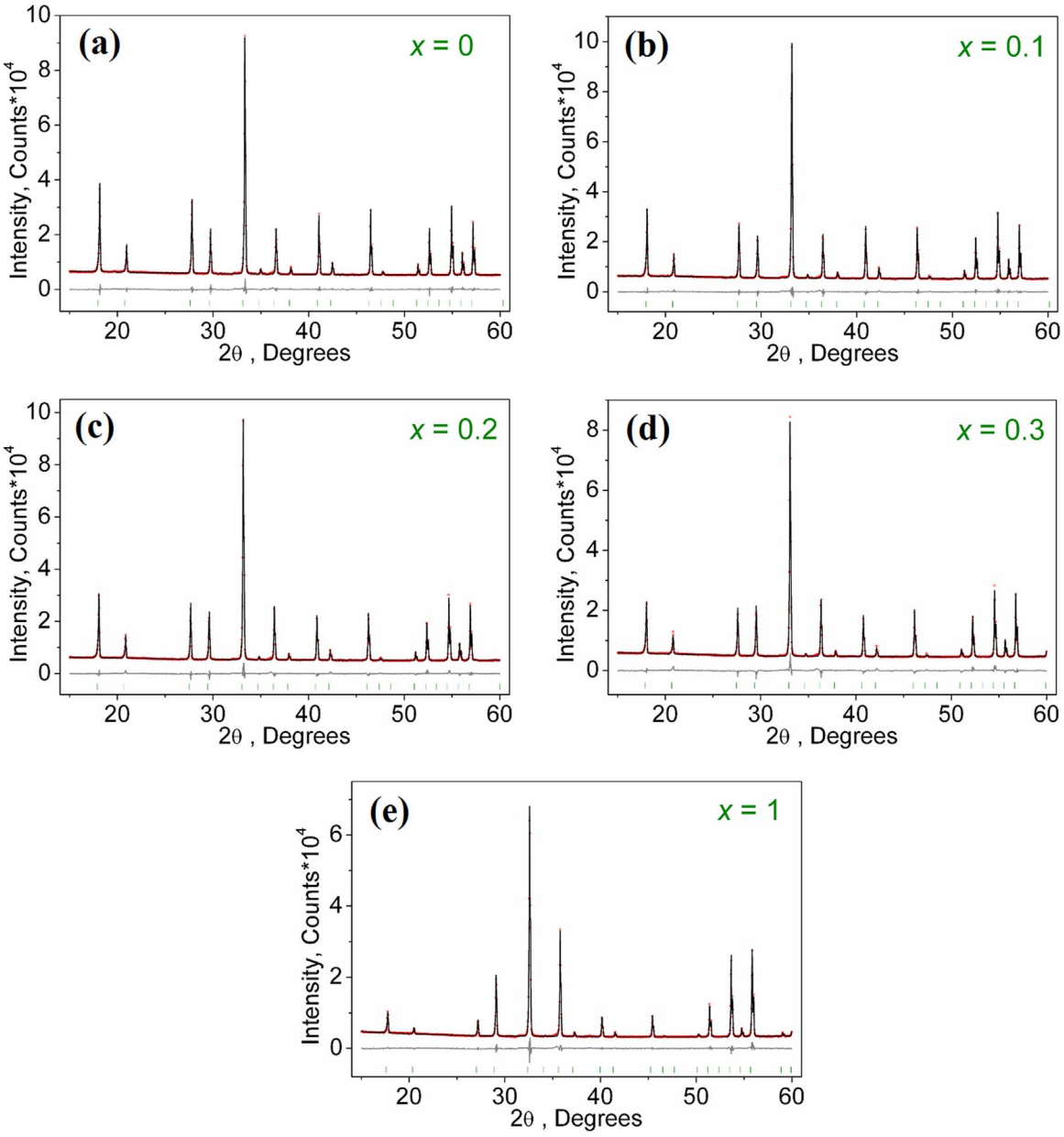

Fig. 2. Observed (black), calculated (red), and difference (gray) XRD profiles for the $(Tb_{0.985}Ce_{0.015})_3(Al_{1-x}Ga_x)_5O_{12}$ phosphors. Green tick marks present the positions of Bragg reflection and the Ga content (x value) is indicated in each part of the figure.

Table 1
Main parameters of processing and refinement of $(Tb_{0.985}Ce_{0.015})_3(Al_{1-x}Ga_x)_5O_{12}$.

Chemical composition	Space group	Cell parameter (Å) Cell volume (Å^3)	Theoretical density (g/cm^3)	R_{wp}, R_p, R_B (%) χ^2
x = 0 $(Tb_{0.985}Ce_{0.015})_3Al_5O_{12}$	*Ia*-3*d*	a = 12.0782 (2) V = 1761.99 (7)	6.059	2.37, 1.73, 0.53 1.96
x = 0.1 $(Tb_{0.985}Ce_{0.015})_3(Al_{0.9}Ga_{0.1})_5O_{12}$	*Ia*-3*d*	a = 12.1023 (2) V = 1772.56 (8)	6.184	2.43, 1.79, 1.07 1.98
x = 0.2 $(Tb_{0.985}Ce_{0.015})_3(Al_{0.8}Ga_{0.2})_5O_{12}$	*Ia*-3*d*	a = 12.1271 (2) V = 1783.50 (7)	6.306	2.76, 2.01, 2.23 2.34
x = 0.3 $(Tb_{0.985}Ce_{0.015})_3(Al_{0.7}Ga_{0.3})_5O_{12}$	*Ia*-3*d*	a = 12.1525 (2) V = 1794.74 (9)	6.425	3.16, 2.24, 3.55 2.43
x = 1 $(Tb_{0.985}Ce_{0.015})_3Ga_5O_{12}$	*Ia*-3*d*	a = 12.3428 (2) V = 1880.37 (9)	7.186	3.12, 2.34, 1.10 2.05

Table 2
Main bond lengths (Å) of the $(Tb_{0.985}Ce_{0.015})_3(Al_{1-x}Ga_x)_5O_{12}$ solid solutions.

x = 0			
Tb—O1	2.478 (5)	Al1—O1	1.939 (5)
Tb—O1^{i}	2.336 (5)	Al2—O1^{i}	1.752 (5)
x = 0.1			
Tb—O	2.471 (5)	Al1—O	1.962 (5)
Tb—O^{i}	2.309 (5)	Al2—O^{i}	1.761 (5)
x = 0.2			
Tb—O	2.478 (6)	Al1—O	1.981 (6)
Tb—O^{i}	2.309 (6)	Al2—O^{i}	1.753 (5)
x = 0.3			
Tb—O	2.483 (7)	Al1—O	1.987 (7)
Tb—O^{i}	2.306 (7)	Al2—O^{i}	1.758 (7)
x = 1			
Tb—O	2.409 (8)	Ga1—O	2.060 (8)
Tb—O^{i}	2.349 (8)	Ga2—O^{i}	1.838 (8)

Symmetry code: (i) − y + 1/4, − x + 1/4, − z + 1/4.

Ga2-O) exhibits little increase in the range of x = 0–0.3 (Fig. 3c). Therefore, it can be predicted that the Ga^{3+} ions prefer to occupy the Al1 site rather than Al2. This is understandable in view that the octahedral Al1 site is much bigger than the tetrahedral Al2 site (Fig. S1), and thus the bigger Ga^{3+} ion preferentially replaces the Al1 site Al^{3+}. It can also be inferred from Figs. 3b and 3c that the Al2 site may start to accept Ga^{3+} only after the Al1 site becomes saturated by the Ga dopant.

The lattice parameter and theoretical density of $(Tb_{0.985}Ce_{0.015})_3(Al_{1-x}Ga_x)_5O_{12}$ are shown in Fig. 4 as a function of the Ga^{3+} concentration. The cell parameter linearly increases with increasing x and observes Vegard's law, implying the already formation of solid solution. The same tendency of change was also observed for the theoretical density. The increasing density is beneficial to scintillation application, since it improves the stopping power and shortens the

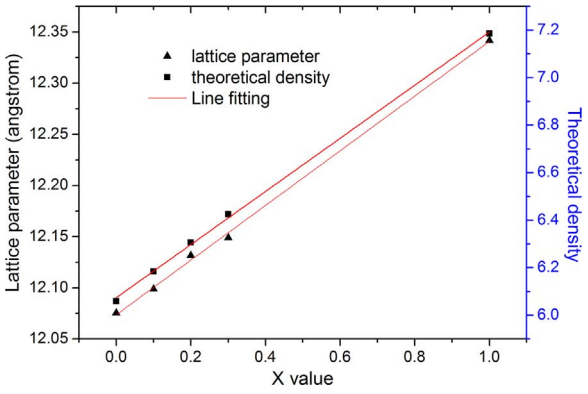

Fig. 4. Lattice parameter and theoretical density of the $(Tb_{0.985}Ce_{0.015})_3(Al_{1-x}Ga_x)_5O_{12}$ solid solutions, as a function of the Ga content (x value).

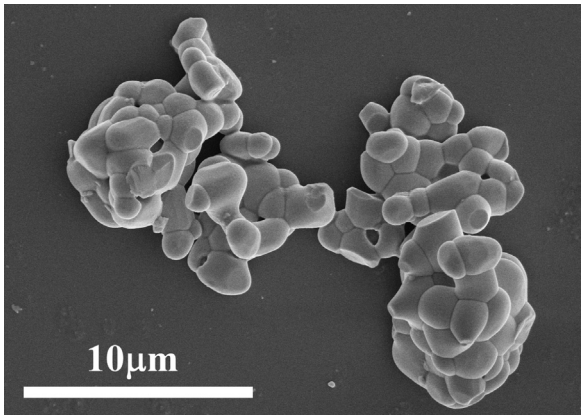

Fig. 5. FE-SEM morphology of the x = 0.3 phosphor powder.

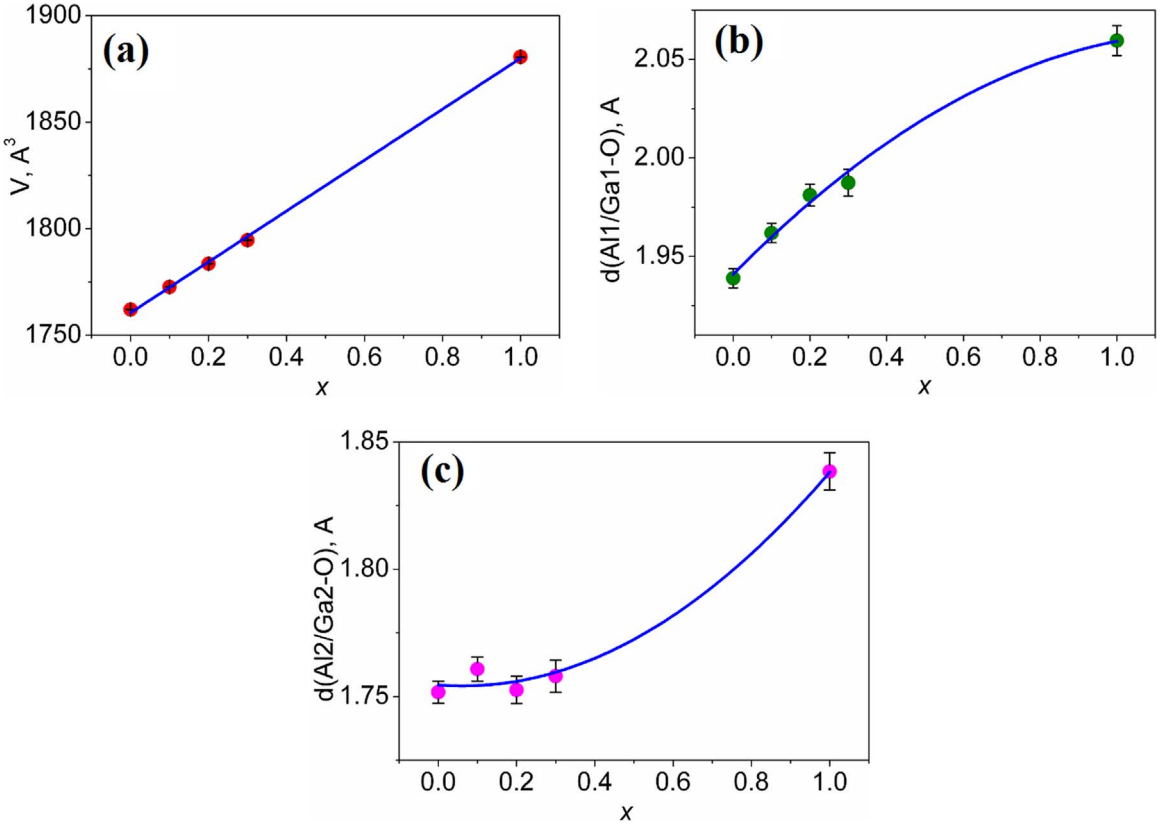

Fig. 3. Cell volume (a) and bond lengths of d(Al1/Ga1-O) (b) and d(Al2/Ga2-O) (c), as a function of the x value.

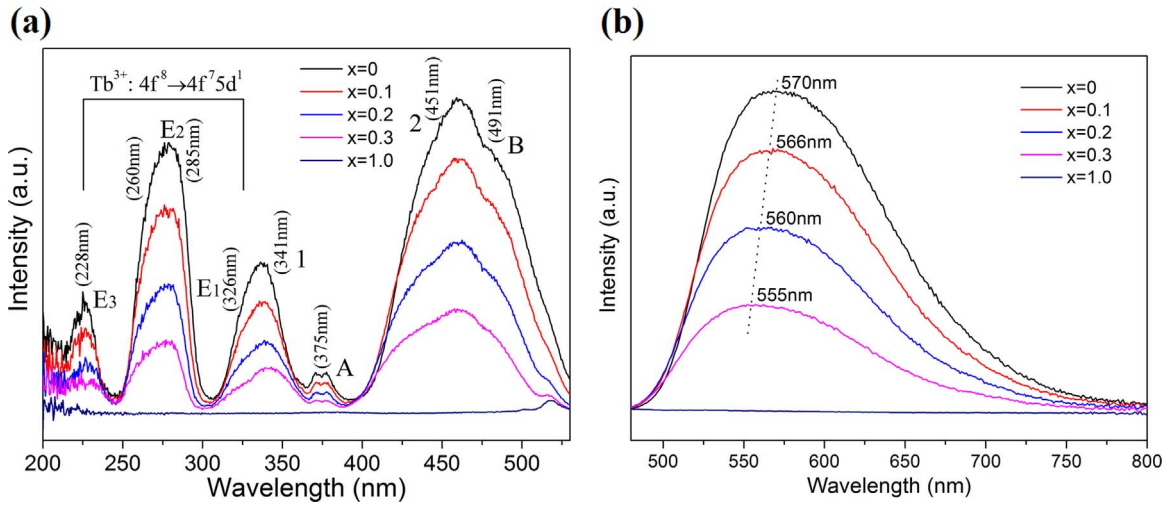

Fig. 6. (a) Excitation spectra of the $(Tb_{0.985}Ce_{0.015})_3(Al_{1-x}Ga_x)_5O_{12}$ phosphors measured by monitoring the Ce^{3+} emission at 570 nm. Numbers 1 and 2 denote the $4f(^2F_{5/2})\rightarrow 5d_2(E_{2g})$ and $4f(^2F_{5/2})\rightarrow 5d_1(E_{2g})$ inter-configurational transitions of Ce^{3+} and letters A and B are for the $^7F_6\rightarrow{}^5D_3$ and $^7F_6\rightarrow{}^5D_4$ intra-$4f^8$ transitions of Tb^{3+}, respectively. (b) Emission spectra of the $(Tb_{0.985}Ce_{0.015})_3(Al_{1-x}Ga_x)_5O_{12}$ phosphors measured under the $4f(^2F_{5/2})\rightarrow 5d_1(E_{2g})$ excitation of Ce^{3+} at 451 nm.

radiation length and thereby reduces the volume and cost of scintillator.

Fig. 5 shows the representative FE-SEM morphology of the $x = 0.3$ phosphor. Though not shown here, all the powders synthesized in this work present similar particle morphologies irrespective of the Ga content. The primary crystallites were observed to have the sizes of ~ 1–3 μm and are sintered together, with the grain boundaries clearly seen. This may indicate that the powder has the favorable sinterability for transparent ceramics fabrication, and sintering studies are now underway.

3.2. Photoluminescence

The photoluminescent properties of TbAG:Ce^{3+} yellow phosphor have been studied [16,25], but very few reports can be found on the effects of Ga^{3+} doping. Fig. 6a shows the excitation spectra of $(Tb_{0.985}Ce_{0.015})_3(Al_{1-x}Ga_x)_5O_{12}$ (λ_{em} = 570 nm), where it is seen that the excitations of both matrix Tb^{3+} and Ce^{3+} activator dominate the whole spectrum in each case. The appearance of Tb^{3+} excitation provides direct evidence of $Tb^{3+}\rightarrow Ce^{3+}$ energy transfer and also experimental support for the matrix excitation used in the field of high-energy scintillators. The three bands centered at ~ 228 nm (E_3), 260 and 285 nm (E_2), and 326 nm (E_1) arise from the $4f^8\rightarrow 4f^7 5d^1$ inter-configurational transitions of Tb^{3+}, while the weak twin-bands in the ~ 360–390 nm region (centered at ~ 375 nm) and the strong band centered at ~ 491 nm are attributed to the $^7F_6\rightarrow{}^5D_3$ and $^7F_6\rightarrow{}^5D_4$ intra-$4f^8$ transitions of Tb^{3+}, respectively [25]. The excitation bands at ~ 341 and 451 nm are due to electronic transitions from the $4f(^2F_{5/2})$ ground state to the second lowest lying $5d_2(E_{2g})$ and lowest-lying $5d_1(E_{2g})$ excited states of Ce^{3+}, respectively [16]. Noteworthy is that Ga doping substantially lowers the excitation intensity and excitation is almost completely quenched at $x = 1.0$. The emission spectra taken under the $4f(^2F_{5/2})\rightarrow 5d_1(E_{2g})$ excitation of Ce^{3+} (λ = 451 nm) are exhibited in Fig. 6b. The emission covers the wide range of ~ 480–800 nm in each case, and the broad emission feature is associated with an overlapping of electronic transitions from the lowest lying $5d_1$ excited state to the 4f ground states, that is, $5d_1(E_{2g})\rightarrow 4f(^2F_{5/2})$ and $5d_1(E_{2g})\rightarrow 4f(^2F_{7/2})$. Ga doping clearly blue shift the emission band and reduces emission intensity, as observed from the intensity of $4f(^2F_{5/2})\rightarrow 5d_1(E_{2g})$ excitation (Fig. 6a), and the emission is almost completely quenched at $x = 1.0$.

It was observed that the $4f(^2F_{5/2})\rightarrow 5d_1(E_{2g})$ lower energy excitation and $4f(^2F_{5/2})\rightarrow 5d_2(E_{2g})$ higher energy excitation bands of Ce^{3+} shift toward higher and lower energies, respectively, with increasing Ga^{3+} incorporation (Fig. S2 and Table S2). This indicates that Ga doping influences the crystal field splitting of Ce^{3+} energy levels, and the strength of splitting decreases with increasing Ga^{3+} content. The magnitude of field splitting can be related to the bond length from the activator to the coordination anion through the equation [26]:

$$Dq = ze^2r^4/6R^5 \quad (1)$$

where Dq is a measure of the energy level splitting, z is the valence of the anion, e is the charge of an electron, r is the radius of the d-orbital wavefunction, and R is the bond length. The increasing lattice parameter at a higher Ga content (Fig. 4) produces a larger R and thus weaker splitting of the Ce^{3+} 5d energy levels according to Eq. (1). This may account for the observed excitation and emission shifts. Additionally, the field splitting and behaviors of Ce^{3+} emission in a garnet structure may be interpreted with the empirical rule of dodecahedral distortion. The Ce^{3+} activator occupies the dodecahedral Tb^{3+}site, with four of the eight Ce–O bonds being shorter and the other four being longer (Table 2), which represents a distorted (compressed) cube. The extent of distortion can be assayed with the ratio of O–O bond distances d_{88} (O–O bond edge shared with an adjacent dodecahedron) and d_{81} (O–O bond edge shared with an adjacent tetrahedron) [27]. A larger d_{88}/d_{81} ratio represents more compression of the cube while decreasing d_{88}/d_{81} ratio represents a closer cubic geometry, and there is an approximately linear relation between the emission/excitation maxima and d_{88}/d_{81} [27]. According to the results of Rietveld refinement, Ga^{3+} preferably occupies the octahedral Al site (Fig. S1) and the Tb(Ce)–O bond length is almost invariable but the Al(Ga)1–O bond length is increasing with increasing Ga concentration (Table 2, Fig. 3b). This implies that the d_{88} bond distance is almost stable but d_{81} is increasing continuously, that is, Ga doping produces a smaller d_{88}/d_{81} ratio. The distorted cubic site is compressed along one axis, resulting in an approximately tetragonal field at the site occupied by Ce^{3+}, and the tetragonal distortion affects the splitting of Ce^{3+} 5d energy levels in garnet [28]. It was reported that more compression will make the lowest 5d energy level [$5d_1(E_{2g})$] move to a lower energy state while the second lowest 5d energy level [$5d_2(E_{2g})$] to a higher energy state. In this work, a higher Ga content gives rise to a smaller d_{88}/d_{81} value, and thus produces a blue shift of both the emission (Fig. 6b) and $4f(^2F_{5/2})\rightarrow 5d_1(E_{2g})$ excitation and meanwhile a red shift of the $4f(^2F_{5/2})\rightarrow 5d_2(E_{2g})$ excitation (Fig. S2, Table S2).

The decreasing emission intensity with increasing Ga content can be ascribed to moving closer of the bottom of the conduction band and the $5d_1$ excited state of Ce^{3+}, which makes the excited electrons more

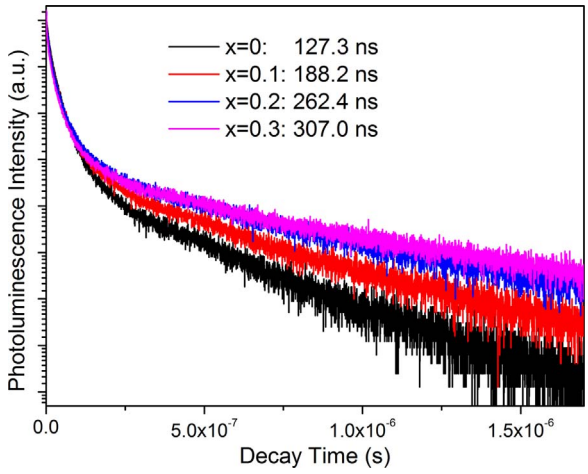

Fig. 7. Fluorescence decay kinetics of the 570 nm emission of $(Tb_{0.985}Ce_{0.015})_3(Al_{1-x}Ga_x)_5O_{12}$ (λ_{ex} = 450 nm), with the derived average lifetimes presented in the figure.

Table 3
A summary of the derived τ_i (ns), the weight (%) of τ_i, B_i, and χ^2 values.

x	τ_1 (weight)	τ_2 (weight)	τ_3 (weight)	B_1	B_2	B_3	χ^2
0	38.9 (53.3)	322.8 (32.7)	9.9 (15.1)	3976.3	299.5	4526.8	1.3
0.1	41.5 (43.5)	397.7 (42.5)	9.4 (14.0)	3377.0	344.1	4833.5	1.5
0.2	43.4 (36.4)	484.9 (50.6)	9.4 (13.0)	3062.3	380.4	5035.1	1.6
0.3	40.1 (34.6)	529.8 (55.2)	7.4 (10.2)	2893.1	349.4	4637.3	1.8

readily jump into the conduction band under thermal fluctuation (thermal activation). This is perceivable by considering that Ga doping lowers the edge of the conduction band [25] and meanwhile reduces crystal field splitting of the Ce^{3+} 5d energy levels as discussed earlier. Additionally, Ga has a higher electronegativity (1.81) than Al (1.61), and thus centroid shift of the Ce^{3+} 5d levels can be affected by Ga doping. The centroid shift is known to be due to a decrease in the inter-electron repulsion [29]. Cations of higher electronegativity tend to bind anion ligands (oxygen in this work) or electrons more strongly, and thus centroid shift decreases with increasing average cation electronegativity of the host lattice [30]. That is, Ga doping may also narrow the energy gap between the bottom of the conduction band and the $5d_1$ excited state by raising the centroid of Ce^{3+} 5d energy levels. Ga doping improves density but deteriorates luminescence intensity of $(Tb_{0.985}Ce_{0.015})_3(Al_{1-x}Ga_x)_5O_{12}$, and thus the optimal composition for practical application should be compromised from these two opposite influences.

Fig. 7 shows decay kinetics of the 570 nm emission of $(Tb_{0.985}Ce_{0.015})_3(Al_{1-x}Ga_x)_5O_{12}$ under 450 nm excitation. All the curves show non-exponential characteristics but can be well fitted with the third-order exponential of $I(t) = B_1\exp(-t/\tau_1) + B_2\exp(-t/\tau_2) + B_3\exp(-t/\tau_3) + A$, where I is the luminescence intensity, A is a constant, B_i (i = 1–3) are pre-exponential constants, t is the delay time, and τ_i (i = 1–3) are the lifetimes for exponential components. The B_i, τ_i, weight of τ_i, and chi-square factor (χ^2) derived via fitting the data with a built-in software of the analyzer are summarized in Table 3. The low χ^2 value indicates good accuracy of fitting in each case. It should be noted that the ultra-fast component (τ_3) with the decay time of a couple of nanoseconds is on the same order of the 1.4 ns pulse duration of the excitation source, and therefore its origin cannot be definitely defined at the moment. The components with the decay times of tens of nanoseconds (τ_1) and hundreds of nanoseconds (τ_2) are most likely related to the intrinsic lifetime of Ce^{3+} emission in the garnet lattice and the energy transfer between Tb^{3+} and Ce^{3+}, respectively [15,16]. Unlike τ_1, τ_2 steadily increases with increasing Ga concentration, which may suggest that more Tb^{3+}/Ce^{3+} energy transfer gets involved, though further study is needed to better understand the energy process. The average lifetime can be calculated with the equation $\tau_{avg} = (B_1\tau_1^2 + B_2\tau_2^2 + B_3\tau_3^2)/(B_1\tau_1 + B_2\tau_2 + B_3\tau_3)$, and the results are included in Fig. 7. It is seen that τ_{avg} substantially increases with increasing Ga doping, mainly owing to the gradually larger τ_2 component.

4. Conclusion

Structure and photoluminescence study of $(Tb_{0.985}Ce_{0.015})_3(Al_{1-x}Ga_x)_5O_{12}$ phosphors (x = 0, 0.1, 0.2, 0.3, and 1.0) revealed the substantial influences of Ga dopant. Rietveld XRD refinement showed that Ga^{3+} preferentially occupies the octahedral Al^{3+} site, which leads to a distortion of the CeO_8 coordination polyhedron. Ga doping was found to (1) linearly increase the cell dimension and theoretical density of the garnet, (2) blue shift the emission and $4f(^2F_{5/2})\rightarrow5d_1(E_{2g})$ excitation and meanwhile red shift the $4f(^2F_{5/2})\rightarrow5d_2(E_{2g})$ excitation of Ce^{3+}, and (3) lower the intensity and elongate the average fluorescence lifetime of Ce^{3+} emission. The observed influence of Ga dopant on Ce^{3+} luminescence can be rationalized by considering the band structure of the host lattice, CeO_8 distortion, and centroid shift and crystal splitting of Ce^{3+} 5d energy levels. It was suggested that centroid shift and crystal field splitting of Ce^{3+} 5d levels and bandgap of the host all decrease towards a higher Ga content.

Acknowledgements

Funded in part by the National Natural Science Foundation of China (Grant nos. 51672039 and 51702020), the Doctoral Research Fund of Liaoning Province (Grant no. 20170520103), and the Russian Foundation for Basic Research (17-52-53031).

Appendix A. Supplementary material

Supplementary data associated with this article can be found in the online version at http://dx.doi.org/10.1016/j.ceramint.2018.02.104.

References

[1] T. Yanagida, K. Kamada, Y. Fujimoto, H. Yagi, T. Yanagitani, Comparative study of ceramic and single crystal Ce:GAGG scintillator, Opt. Mater. 35 (2013) 2480–2485.
[2] Y.T. Wu, M. Nikl, V. Jary, G.H. Ren, Thermally induced ionization of $5d_1$ state of Ce^{3+} ion in $Gd_3Ga_3Al_2O_{12}$ host, Chem. Phys. Lett. 574 (2013) 56–60.
[3] P. Prusa, K. Kamada, M. Nikl, A. Yoshikawa, J.A. Mares, Light yield of $(Lu,Y,Gd)_3Al_2Ga_3O_{12}$:Ce garnets, Radiat. Meas. 56 (2013) 62–65.
[4] J.L. Luo, Y.T. Wu, G.Q. Zhang, H.J. Zhang, G.H. Ren, Composition-property relationships in $(Gd_{3-x}Lu_x)(Ga_yAl_{5-y})O_{12}$:Ce (x = 0–3 and y = 0–4) multicomponent garnet scintillators, Opt. Mater. 36 (2013) 476–481.
[5] E. Mihóková, K. Vávrů, K. Kamada, V. Babin, A. Yoshikawa, M. Nikl, Deep trapping states in cerium doped $(Lu,Y,Gd)_3(Ga,Al)_5O_{12}$ single crystal scintillators, Radiat. Meas. 56 (2013) 98–101.
[6] P. Korenbos, Electronic structure and optical properties of the lanthanide activated $RE_3(Al_{1-x}Ga_x)_5O_{12}$ (RE = Gd, Y, Lu) garnet compounds, J. Lumin. 134 (2013) 310–318.
[7] E. Zych, D. Hreniak, W. Strek, Spectroscopic properties of Lu_2O_3/Eu^{3+} nanocrystalline powders and sintered ceramics, J. Phys. Chem. B 106 (15) (2002) 3805–3812.
[8] S.J. Duclos, C.D. Greskovich, R.J. Lyons, J.S. Vartuli, D.M. Hoffman, R.J. Riedner, M.J. Lynch, Development of the Hilight™ scintillator for computed tomography medical imaging, Nucl. Instrum. Methods A 505 (1-2 1) (2003) 68–71.
[9] J.W. Dai, Y.B. Pan, W. Wang, W. Luo, T.F. Xie, H.M. Kou, J. Li, Fabrication of $Tb_3Al_5O_{12}$ transparent ceramics using co-precipitated nanopowders, Opt. Mater. 73 (2017) 38–44.
[10] J.W. Dai, Y.B. Pan, H.H. Chen, T.F. Xie, H.M. Kou, J. Li, Synthesis of Tb_4O_7 nanopowders by the carbonate-precipitation method for $Tb_3Al_5O_{12}$ magneto-optical ceramics, Opt. Mater. 73 (2017) 706–711.
[11] J.W. Dai, Y.B. Pan, H.H. Chen, T.F. Xie, H.M. Kou, J. Li, Fabrication of $Tb_3Al_5O_{12}$ transparent ceramics using co-precipitated nanopowders: the influence of ammonium hydrogen carbonate to metal ions molar ratio, Ceram. Int. 43 (2017) 14457–14463.
[12] E.G. Villora, P. Molina, M. Nakamura, K. Shimamura, T. Hatanaka, A. Funaki, K. Naoe, Faraday rotator properties of $\{Tb_3\}[Sc_{1.95}Lu_{0.05}](Al_3)O_{12}$, a highly transparent terium-garnet for visible-infrared optical isolators, Appl. Phys. Lett. 99 (2011) 011111.
[13] Y.B. Chen, M.L. Gong, G. Wang, Q. Su, High efficient and low color-temperature

white light-emitting diodes with $Tb_3Al_5O_{12}:Ce^{3+}$ phosphor, Appl. Phys. Lett. 91 (2007) 071117.
[14] H.D. Luo, J. Liu, X. Zheng, B. Xu, Y.M. Lu, L.X. Han, K.X. Ren, X.B. Yu, Synthesis and luminescence properties of Mg-Si co-doped $Tb_3Al_5O_{12}:Ce^{3+}$ phosphors with blue excitation for white LEDs, J. Am. Ceram. Soc. 95 (2012) 3582–3587.
[15] Y. Zorenko, T. Voznyak, V. Vistovsky, T. Zorenko, S. Nedilko, M. Batentschuk, A. Osvet, A. Winnacker, G. Zimmerer, V. Kolobanov, D. Spassky, Energy transfer to Ce^{3+} Ions in $Tb_3Al_5O_{12}$:Ce single crystalline films, Radiat. Meas. 42 (2007) 648–651.
[16] J. Bi, J.-G. Li, Q. Zhu, J.L. Chen, X.D. Li, X.D. Sun, B.-N. Kim, Y. Sakka, Yellow-emitting $(Tb_{1-x}Ce_x)_3Al_5O_{12}$ phosphor powder and ceramic ($0 \le x \le 0.05$): phase evolution, photoluminescence, and the process of energy transfer, Ceram. Int. 43 (2017) 8163–8170.
[17] M. Fasoli, A. Vedda, M. Nikl, C. Jiang, B.P. Uberuaga, D.A. Andersson, K.J. McClellan, C.R. Stanek, Band-gap engineering for removing shallow traps in rare-earth $Lu_3Al_5O_{12}$ garnet scintillators using Ga^{3+} doping, Phys. Rev. B 84 (2011) 081102(R).
[18] K. Kamada, T. Endo, K. Tsutsumi, Composition engineering in cerium-doped $(Lu,Gd)_3(Ga,Al)_5O_{12}$ single-crystal scintillators, Cryst. Growth Des. 11 (2011) 4484–4490.
[19] K. Kamada, T. Yanagida, J. Pejchal, M. Nikl, T. Endo, et al., Scintillator-oriented combinatorial search in Ce-doped $(Y,Gd)_3(Ga,Al)_5O_{12}$ multicomponent garnet compounds, J. Phys. D: Appl. Phys. 44 (2011) 505104.
[20] Y.V. Zorenko, Mechanism of dissipation of the excitation energy in garnet oxides doped with rare-earth ions with 4f-5d transitions, Opt. Spectrosc. 88 (2000) 551–553.
[21] M. Nikl, A. Vedda, V.V. Laguta, Energy transfer and storage processes in scintillators: the role and nature of defects, Radiat. Meas. 42 (2007) 509–514.
[22] J. Bi, J.-G. Li, W.M. Guan, J.L. Chen, X.D. Sun, Co-precipitation synthesis and photoluminescence properties of Ce^{3+} activated terbium aluminum garnet $(Tb_{1-x}Ce_x)_3Al_5O_{12}$ ($0 \le x \le 0.05$) yellow phosphors, Key Eng. Mater. 602–603 (2014) 1028–1033.
[23] Bruker AXS TOPAS V4: General profile and structure analysis software for powder diffraction data. User's Manual, Bruker AXS, Karlsruhe, Germany, 2008.
[24] R.D. Shannon, Revised effective ionic radii and systematic studies of interatomic distances in halides and chalcogenides, Acta Cryst. A 32 (5) (1976) 751–767.
[25] Y. Zorenko, V. Gorbenko, T. Voznyak, T. Zorenko, B. Kuklinski, R.T. Matysyak, M. Grinberg, Luminescence properties of phosphors based on $Tb_3Al_5O_{12}$ (TbAG) terbium–aluminum garnet, Opt. Spectrosc. 106 (2009) 365–374.
[26] P.D. Rack, P.H. Holloway, The structure, device physics, and material properties of thin film electroluminescent displays, Mater. Sci. Eng. R 21 (1998) 171–219.
[27] J.L. Wu, G. Gundiah, A.K. Cheetham, Structure-property correlations in Ce-doped garnet phosphors for use in solid state lighting, Chem. Phys. Lett. 441 (2007) 250–254.
[28] D.J. Robbins, The effects of crystal field and temperature on the photoluminescence excitation efficiency of Ce^{3+} in YAG, J. Electrochem. Soc. 126 (1979) 1550–1555.
[29] N.C. George, K.A. Denault, R. Seshadri, Phosphors for solid-state white lighting, Annu. Rev. Mater. Res. 43 (2013) 481–501.
[30] P. Dorenbos, J. Andriessen, C.W.E. van Eijk, $4f^{n-1}5d$ centroid shift in lanthanides and relation with anion polarizability, covalency, and cation electronegativity, J. Solid State Chem. 171 (2003) 133–136.